https://doi.org/10.5194/egusphere-2026-2292
Preprint. Discussion started: 2 June 2026

Wave-phase-aware model implementation in WRF-LES v3.8.1 for turbulence-resolving simulations of turbulent flow over monochromatic waves

Baris Kale [1], Mohammadreza Asadbeigi [2], Aditya K. Aiyer [2], and Michael F. Howland [1]

[1]Department of Civil and Environmental Engineering, Massachusetts Institute of Technology, Cambridge, MA, USA
[2]Department of Mechanical Engineering and Mechanics, Lehigh University, Bethlehem, PA, USA

Correspondence: Baris Kale (bkale@mit.edu)

Abstract. In simulations of turbulent marine atmospheric flows, wind-wave interactions are commonly represented using bulk, wave-phase-averaged parameterizations, which can introduce errors across different wave conditions due to their inability to capture phase-dependent processes. In scale-resolving large-eddy simulations (LES) or direct numerical simulations (DNS), wave-phase-resolved approaches explicitly represent wave geometry, but at a substantial computational cost. To bridge this gap, recent developments in wave-phase-aware models incorporate phase-dependent effects at reduced cost, often by leveraging canopy-stress analogies originally developed for atmospheric boundary layer flows over rough surfaces. However, differences in model implementation across numerical frameworks have hindered direct comparison of the predictions from these different wave representations in LES. In this study, we implement two wave-phase-aware models, the Wave Drag Model (WDM) and the Windward Potential Flow Model (WPM), within a unified LES framework using WRF-LES, and compare them against a wave-phase-resolved moving-wave (MOW) model under identical forcing conditions, enabling a consistent assessment of the trade-offs between computational efficiency and physical fidelity. The wave-phase-aware models reproduce mean velocity profiles with typical deviations of $\mathcal{O}(8\%\text{-}11\%)$, with best agreement for low steepness ($ak = 0.10$) across all wave ages, while discrepancies increase for steeper waves at high wave age. They capture key momentum transfer behavior, including momentum reversal from the waves to the airflow, but underestimate wave-induced velocity fluctuations by about one order of magnitude relative to the wave-phase-resolved model. The wave-phase-aware models implemented in WRF-LES v3.8.1 are made publicly available to facilitate reproducibility and broader community use.

1 Introduction

Air-sea exchange processes are a key component of atmospheric modeling systems, yet in most operational frameworks they are represented using bulk, phase-averaged parameterizations in which the ocean surface is treated as an effective rough boundary. In such approaches, wave effects are incorporated implicitly through aerodynamic roughness relations, including the Charnock relation (Charnock, 1955) and sea-state-dependent formulations based on wave age, steepness, or wind-wave misalignment (Donelan, 1990; Taylor and Yelland, 2001; Porchetta et al., 2019). Surface fluxes are typically computed using Monin-Obukhov

https://doi.org/10.5194/egusphere-2026-2292
Preprint. Discussion started: 2 June 2026

similarity theory (MOST) with bulk transfer coefficients, as implemented in COARE-type schemes (Fairall et al., 2003). While computationally efficient, these formulations do not explicitly represent wave geometry or phase-dependent flow structure.

To address this limitation, a hierarchy of modeling approaches has emerged. At the high-fidelity end, wave-phase-resolved models explicitly represent the evolving wave surface and its interaction with the airflow in a one-way-coupled framework, but remain computationally expensive for practical application (Hara and Sullivan, 2015; Sullivan et al., 2018; Husain et al., 2022; Zhu et al., 2023). Intermediate approaches, commonly referred to as wave-phase-aware models, aim to retain essential phase-dependent effects while maintaining tractability (Aiyer et al., 2023; Ayala et al., 2024). These models typically represent waves as distributed momentum sinks or pressure perturbations, drawing on canopy-stress analogies developed for atmospheric boundary layer flows over rough surfaces (Anderson, 2010; Arthur et al., 2019).

The Wave Drag Model (WDM) of Aiyer et al. (2023) is one wave-phase-aware model that computes wave-induced momentum transfer based on the airflow velocity relative to the wave phase speed, applied selectively over windward-facing surfaces. An alternative wave-phase-aware model is the Windward Potential Flow Model (WPM) of Ayala et al. (2024), which prescribes enhanced pressure over windward slopes using a potential flow analogy. In both approaches, unresolved small-scale wave effects are represented through a MOST-based wall model formulated in terms of a background roughness length, $z_{0,b}$.

Despite recent developments, direct comparison between wave-phase-aware and wave-phase-resolved approaches has been limited by differences in numerical implementation, turbulence closure, and forcing conditions across studies. These inconsistencies obscure the role of model formulation and complicate assessment of their relative performance.

Systematically interrogating wind-wave interactions across this modeling hierarchy requires a framework that resolves atmospheric turbulence while allowing controlled modification of lower boundary representations. LES provides this capability; here, we use the widely adopted Weather Research and Forecasting (WRF-LES) framework (Skamarock and Klemp, 2008) as a common platform. Within this framework, we implement a hierarchy of air-sea interaction models spanning different levels of physical fidelity: a wave-phase-resolved moving-boundary formulation following Zhu et al. (2023), and wave-phase-aware models based on Aiyer et al. (2023) and Ayala et al. (2024). Embedding these models within the same LES framework under identical turbulence and large-scale forcing enables direct and controlled comparison, eliminating confounding methodological differences and allowing quantitative assessment of the trade-offs between computational efficiency and physical fidelity. The moving-wave (MOW) model, previously incorporated and validated within this codebase (Zhu et al., 2023), is used here as a reference solution without additional verification, against which the wave-phase-aware models are evaluated across a range of wave regimes using mean flow and turbulence statistics.

The remainder of this paper is organized as follows. Section 2 describes the numerical framework. The implementation details of the wave-phase-aware models are presented in Section 3, while the simulated wave regimes are introduced in Section 4. The WRF-LES model configuration is detailed in Section 5. Results from both wave-phase-resolved and wave-phase-aware simulations across a range of wave ages and steepness values are presented and discussed in Section 6. Finally, Section 7 summarizes the main findings and outlines directions for future work.

https://doi.org/10.5194/egusphere-2026-2292
Preprint. Discussion started: 2 June 2026

2 Numerical framework

2.1 WRF-LES model

The WRF-LES framework is a nonhydrostatic, compressible atmospheric model configured in LES mode to resolve microscale turbulence (Skamarock and Klemp, 2008). In LES configuration, it solves the Favre-filtered continuity and momentum equations,

$$\frac{\partial u_i}{\partial x_i} = 0,$$
$$\frac{\partial u_i}{\partial t} = -\frac{\partial u_i u_j}{\partial x_j} - \frac{1}{\rho}\frac{\partial p}{\partial x_i} - \frac{\partial \tau_{ij}}{\partial x_j} + f_c \epsilon_{ij3}(u - U_{gj}) + \mathcal{F}_i \tag{1}$$

where u_i are the resolved velocity components, with $i, j = 1, 2, 3$ corresponding to the longitudinal, lateral and vertical directions, respectively, p is the resolved pressure, ρ is the resolved density, f_c is the Coriolis parameter, U_{g_j}, with $j = 1, 2$, are the longitudinal and lateral components of geostrophic wind velocity in horizontal space, ϵ_{ij3} is the alternating unit tensor, $\mathcal{F}_i$ is a forcing term (e.g., additional forces induced by the waves) and x_i denotes the spatial coordinates. No viscous effects are resolved near the surface due to high Reynolds number condition. It is important to note that all flow variables represent LES-filtered quantities, whereas the quantities denoted by $(\tilde{\cdot})$ correspond to wave-induced components, while the $(\hat{\cdot})$ operator indicates an additional filtering at the test-filter scale, 2Δ, and $(\bar{\cdot})$ refers to temporal averaging throughout the manuscript.

The subfilter-scale (SFS) stress tensor is defined as

$$\tau_{ij} = \overline{u_i u_j} - \overline{u}_i \overline{u}_j. \tag{2}$$

Closure of the system is achieved through an equation of state for pressure and a prognostic relation for the geopotential, $\phi = g x_3$, where $x_3 = z$ denotes the vertical coordinate. Spatial discretization employs a staggered Arakawa C-grid with a terrain-following hydrostatic-pressure vertical coordinate defined as

$$\zeta = \frac{p - p_t}{\mu}. \tag{3}$$

Here, $\mu = p_s - p_t$ denotes the difference between the hydrostatic pressure at the surface, p_s, and the hydrostatic pressure at the top of the domain, p_t.

WRF integrates the compressible Navier–Stokes equations within a generalized pressure-based curvilinear coordinate framework. This formulation is obtained by transforming the physical coordinates (x, y, z, t) into a terrain-following hydrostatic-pressure coordinate system (ξ, η, ζ, τ) through an algebraic mapping. In the transformed system, $\tau = t$ denotes time, while $\xi = x$ and $\eta = y$ correspond to the horizontal curvilinear coordinates. In WRF, the equations of motion are cast in a conservative flux form, where the conservative flux vector is expressed as

$$\mathbf{U} = \mu(u, v, w) = (U, V, W), \tag{4}$$

and the cross-coordinate flux is given by

$$\Omega = \mu \frac{d\zeta}{dt}. \tag{5}$$

https://doi.org/10.5194/egusphere-2026-2292
Preprint. Discussion started: 2 June 2026

Time integration is performed using a third-order Runge–Kutta scheme, while horizontal and vertical advection terms are discretized using fifth- and third-order finite-difference schemes, respectively. In the default WRF-LES configuration, the numerical discretization provides implicit filtering at scales comparable to the grid resolution, suppressing high-wavenumber content without the need for an explicit filter.

2.2 Description of the wave-phase-resolved and wave-phase-aware models

In this study, we implement and evaluate two wave-phase-aware models (WDM and WPM) within the WRF-LES framework, using a wave-phase-resolved approach (MOW) as a reference. The MOW model prescribes a dynamically evolving wave surface and explicitly resolves the flow response, whereas WDM and WPM retain horizontal phase information while parameterizing unresolved vertical structure and small-scale processes through wall-modeling concepts. Details of each model are provided below.

2.2.1 Moving-wave Model (MOW)

To explicitly resolve wave geometry in WRF-LES, a moving lower boundary is introduced to represent the evolving wave surface. As described in Zhu et al. (2023), implementing a moving bottom in WRF involves two main steps: defining the appropriate boundary conditions and updating the hydrostatic balance at each time step as the surface moves. The water surface is specified as $z = h$, which adjusts the computational grid near the lower boundary to conform to the prescribed wave shape. Applying the kinematic boundary condition at the air-sea interface and assuming continuity of vertical velocity, the vertical motion of the surface is taken to be equal to the vertical air velocity at the interface, such that

$$w|_{z=h} = \frac{dh}{dt} = \frac{\partial h}{\partial \tau} + u|_{\zeta=1}\frac{\partial h}{\partial \xi} + v|_{\zeta=1}\frac{\partial h}{\partial \eta}. \tag{6}$$

Using the prognostic geopotential equation, $\phi = gz$, Equation (6) can be rearranged as follows:

$$gw|_{z=h} = \left(\frac{\partial \phi}{\partial \tau} + u\frac{\partial \phi}{\partial \xi} + v\frac{\partial \phi}{\partial \eta}\right)\Bigg|_{\zeta=1}. \tag{7}$$

At the bottom boundary, the cross-coordinate flux defined in Equation (5) satisfies the condition $\Omega\big|_{\zeta=1} = 0$. For a rough, moving lower surface, the default quadratic drag law boundary condition in WRF-LES is modified to account for surface motion by computing the surface stress based on the air velocity relative to the moving water surface, such that

$$\mathbf{u}_r = \mathbf{u} - \mathbf{u}_s, \tag{8}$$

where $\mathbf{u}_s$ is the wave surface orbital velocity at $z = h$. The components of the relative velocity parallel to the local water surface are defined as

$$u_{||} = \frac{u_r + w_r\,(\partial h/\partial \xi)}{\sqrt{1 + (\partial h/\partial \xi)^2}}, \tag{9a}$$

$$v_{||} = \frac{v_r + w_r\,(\partial h/\partial \eta)}{\sqrt{1 + (\partial h/\partial \eta)^2}}, \tag{9b}$$

https://doi.org/10.5194/egusphere-2026-2292
Preprint. Discussion started: 2 June 2026

where the unresolved wall stress is given by

$$\tau_{i3}\big|_{\text{wall}} = C_d |\mathbf{u}_r| \mathbf{u}_{||,i}, \qquad \text{for } i = 1, 2. \tag{10}$$

The drag coefficient, C_d, is determined such that the horizontal velocity in the bottom-most grid cell ($z = h + \Delta z/2$) satisfies the logarithmic velocity profile:

$$C_d = \left[\frac{\kappa}{\ln\left((\Delta z/2)/\, z_{0,b}\right)} \right]^2, \tag{11}$$

where $\kappa = 0.4$ is the von Kármán constant, and $\Delta z/2$ is the first off-wall grid point. In Equation (11), the background surface roughness length scale, $z_{0,b}$, which represents the roughness associated with the unresolved, small-scale features on the wave, is specified directly by the user.

In addition to the wave boundary conditions described above, the original WRF formulation treats hydrostatic variables as time-invariant because they are defined relative to a static lower boundary. However, in the presence of surface waves the grid elevation varies with the wave motion, which in turn alters the associated hydrostatic variables. In the moving bottom implementation, this temporal variation is handled by a hydrostatic rebalancing procedure in which the hydrostatic variables at the surface are recomputed at the end of each time step to reflect the updated elevation, and the resulting rebalanced hydrostatic and perturbation fields are then used to evaluate the governing equations at the next time step. The implementation details of the coupled WRF-LES with a moving surface wave boundary condition are presented in Zhu et al. (2023).

2.2.2 Wave Drag Model (WDM)

The Wave Drag Model (WDM) of Aiyer et al. (2023) represents wind-wave momentum exchange in LES without resolving the instantaneous wave phase. It extends the surface gradient drag formulation of Anderson (2010) to moving waves by relating drag to the incoming momentum flux interacting with the wave frontal area. Complete details and derivation of WDM are given in Aiyer et al. (2023).

In WDM, the relative velocity between the airflow and the wave phase speed,

$$\mathbf{u}_r = \mathbf{u} - c\mathbf{e}_i, \qquad \text{for } i = 1, 2, \tag{12}$$

is used to define the momentum flux incident on the wave surface, where $\mathbf{u}$ is the wind velocity vector evaluated at $z = \Delta z/2$, c is the wave phase speed, and $\mathbf{e}_i$ is the unit vector in the direction of wave propagation. This relative velocity is used to calculate the incoming momentum flux onto the wave surface, which is the basis for the drag force. The drag is assumed to scale with the square of the relative velocity and with the frontal area presented by the surface, which is quantified through the local surface gradient. The instantaneous drag force per unit area is then formulated as

$$F_{d,i}^{\text{WDM}} = -C_D \frac{\rho}{\Delta z} u_i U^{\Delta} \left(n_k \cdot \frac{\partial h}{\partial x_k} \right) H\left(n_k \cdot \frac{\partial h}{\partial x_k} \right), \qquad \text{for } i, k = 1, 2, \tag{13}$$

where C_D is the drag coefficient associated with the wind-wave momentum exchange, $n_k = \mathbf{u}_r / U^{\Delta}$ is the normalized relative velocity, and $U^{\Delta} = \sqrt{(u - c_x)^2 + (v - c_y)^2}$ is the magnitude of velocity relative to the wave propagation speed. c_x and c_y are

https://doi.org/10.5194/egusphere-2026-2292
Preprint. Discussion started: 2 June 2026

the components of the wave propagation speed in the streamwise and spanwise directions, respectively. In Equation (13), the air velocity, u_i, is the velocity at the first grid point above surface, and the Heaviside function, $H(x)$, restricts the drag forcing to regions of the wave where the airflow actually impinges on the surface (i.e., windward faces), and the drag is only applied when $H(n_k \cdot \partial h/\partial x_k) > 0$.

The steepness-dependent drag coefficient, C_D, is given as

$$C_D = \frac{P}{1+Q(ak)^2}ak, \tag{14}$$

where the coefficients are set to $P = 1.2$ and $Q = 6$ in Aiyer et al. (2023).

The total wall stress can be expressed as the sum of contributions from the unresolved and resolved wave-induced stresses given by Equation (15). The first term represents the modeled smooth wall (unresolved) stress, while the second term accounts for the resolved wave field computed using the wave drag model (WDM):

$$\tau_{i3}^{\text{Total}} = \tau_{i3}\big|_{\text{wall}} + \frac{\Delta z}{\rho} F_{d,i}^{\text{WDM}}, \qquad \text{for } i = 1,2, \tag{15}$$

where the unresolved wall stress is modeled based on a presumed logarithmic velocity in the surface layer from MOST as

$$\tau_{i3}\big|_{\text{wall}} = \left[\frac{\kappa}{\log\left(\frac{\Delta z/2-h}{z_{0,b}}\right)}\right]^2 \hat{\mathbf{u}}_r \hat{U}_{\text{LES}}, \qquad \text{for } i = 1,2, \tag{16}$$

with $\hat{U}_{\text{LES}} = \sqrt{\hat{u}_r^2 + \hat{v}_r^2}$ denoting the magnitude of the tangential wind velocity relative to the wave surface. The relative velocity components are defined as $\hat{u}_r = \hat{u} - u_s$ and $\hat{v}_r = \hat{v} - v_s$, evaluated at the first grid point above the surface ($\Delta z/2$). Here, u_s and v_s represent the wave surface orbital velocities in the streamwise and spanwise directions, respectively. The small-scale smooth surface roughness length scale for WDM, $z_{0,b}$, is given as

$$z_{0,b} = 0.11\frac{\nu}{u_*}, \tag{17}$$

where 0.11 corresponds to the smooth roughness scale Reynolds number for low wind speeds over smooth ocean surfaces, u_* is the surface friction velocity, and $\nu \approx 1.5 \times 10^{-5}\ \text{m}^2\,\text{s}^{-1}$ denotes the kinematic viscosity of air.

2.2.3 Windward Potential Flow Model (WPM)

The Windward Potential Flow Model (WPM) provides a phase-dependent parameterization of wind-wave momentum exchange for LES by approximating the surface as piecewise planar segments and modeling airflow as ideal potential flow over an inclined surface in a frame moving with the local wave phase speed, C_i. For a given wave geometry, C_i is obtained from the spatiotemporal derivatives of the surface elevation, h, as follows; complete details and derivation are provided in Ayala et al. (2024).

$$C_i = -\frac{\partial h}{\partial t}\frac{\partial h}{\partial x_i}\frac{1}{|\nabla h|^2}, \qquad \text{for } i = 1,2. \tag{18}$$

https://doi.org/10.5194/egusphere-2026-2292
Preprint. Discussion started: 2 June 2026

The WPM formulation assumes that significant pressure drag on the flow arises primarily from wave surface segments that face the incoming wind, while pressure contributions from the opposite (leeward) side are omitted based on the assumption that the flow there tends to separate or be near separation and thus contributes minimally to the overall drag (Ayala et al., 2024). The instantaneous drag force per unit area in WPM is then expressed as

$$F_{d,i}^{\mathrm{WPM}} = -\frac{\rho}{\Delta z}\frac{1}{\pi}\left|(\mathbf{u}-\mathbf{C})\cdot\frac{\nabla h}{|\nabla h|}\right|^2 |\nabla h|^2 H\Big((\mathbf{u}-\mathbf{C})\cdot\nabla h\Big)\frac{\nabla h}{|\nabla h|}, \qquad \text{for } i=1,2. \tag{19}$$

As in WDM, the WPM formulation resolves horizontal wave geometry in LES while leaving the vertical structure unresolved. Effects of small-scale roughness (e.g., ripples or subfilter waves) are represented using a MOST-based wall stress. This yields a surface stress boundary condition that inherently depends on the instantaneous wave slope and relative wind speed, without requiring empirically tuned coefficients, as the pressure drag is derived mechanistically from ideal flow over forward-facing segments of the moving surface.

Unlike the WDM, which represents unresolved wave effects simply using a background roughness length for smooth surfaces, WPM is coupled with a more general MOST-based wall model inspired by Meneveau (2020). This formulation provides a unified fit across smooth, transitional, and rough flow regimes based on a generalized Moody diagram, allowing the wall stress in wall-modeled LES to be computed without explicitly specifying a fixed roughness length. Using this wall model, the stress due to unresolved, small-scale waves is then expressed as

$$\tau_{i3}|_{\mathrm{wall}} = \frac{1}{2}c_f^{\mathrm{wm}}(\mathrm{Re}_\Delta, z_{0,b}/\Delta)\hat{U}_{\mathrm{LES}}^{\Delta}\hat{\mathbf{u}}_r^{\Delta}, \qquad \text{for } i=1,2. \tag{20}$$

Here, $\hat{\mathbf{u}}_r^{\Delta} = \hat{\mathbf{u}}^{\Delta} - \mathbf{u}_s$ denotes the relative velocity used in the WPM formulation, analogous to the relative wind velocity in the WDM model (Equation (12)), where $\hat{\mathbf{u}}^{\Delta}$ is the LES input velocity at the wall-model reference height relative to the moving surface and $\mathbf{u}_s$ is the wave surface orbital velocity vector. In WPM, the input velocity for the wall model is taken from the third grid point above the surface, at $\Delta = 2.5\,\Delta z$, whereas in the WDM formulation it is taken at the first grid point off the wall. The wall model friction factor, c_f^{wm}, entering the wall model is defined as a function of the Reynolds number based on the LES velocity at height Δ, $\mathrm{Re}_\Delta = U_{\mathrm{LES}}^{\Delta}\Delta/\nu$. It also depends on the dimensionless roughness ratio, $z_{0,b}/\Delta$, which vanishes in the smooth limit and becomes independent of Re_Δ in the fully rough regime. The friction factor is then given by

$$c_f^{\mathrm{wm}}(\mathrm{Re}_\Delta, z_{0,b}/\Delta) = 2\left[\left(\frac{\mathrm{Re}_{\tau\Delta}^{s}}{\mathrm{Re}_\Delta}\right)^6 + \left(\frac{1}{\kappa}\log(\Delta/z_{0,b})\right)\right]^{1/3}, \tag{21}$$

where $\mathrm{Re}_{\tau\Delta}^{s} = u_*^s/\nu$ is the wall stress friction Reynolds number for a smooth surface, which is given as

$$\mathrm{Re}_{\tau\Delta}^{s}(\mathrm{Re}_\Delta) = 0.005^{\beta_1-1/2}\mathrm{Re}_\Delta^{\beta_1}[1+(0.005\mathrm{Re}_\Delta)^{-\beta_2}]^{(\beta_1-1/2)/\beta_2}, \tag{22}$$

where $\beta_1 = (1+0.155\mathrm{Re}_\Delta^{-0.03})^{-1}$ and $\beta_2 = 1.7-(1+36\mathrm{Re}_\Delta^{-0.75})^{-1}$.

The total surface stress is obtained by summing the contributions from the unresolved surface roughness and the resolved wave-induced pressure drag. The first term corresponds to the equilibrium wall stress associated with small, unresolved wave features, while the second term represents the resolved drag due to forward-facing wave geometry computed using WPM.

https://doi.org/10.5194/egusphere-2026-2292
Preprint. Discussion started: 2 June 2026

Accordingly, the total wall stress can be written as

$$\tau_{i3}^{\text{Total}} = \tau_{i3}\big|_{\text{wall}} + \frac{\Delta z}{\rho} F_{d,i}^{\text{WPM}}, \qquad \text{for } i = 1, 2. \tag{23}$$

In Equation (21), the background surface roughness length scale, $z_{0,b}$, may be specified directly by the user, or it can be computed using Equation (15) of Ayala et al. (2024).

3 Wave-phase-aware model implementation in WRF-LES

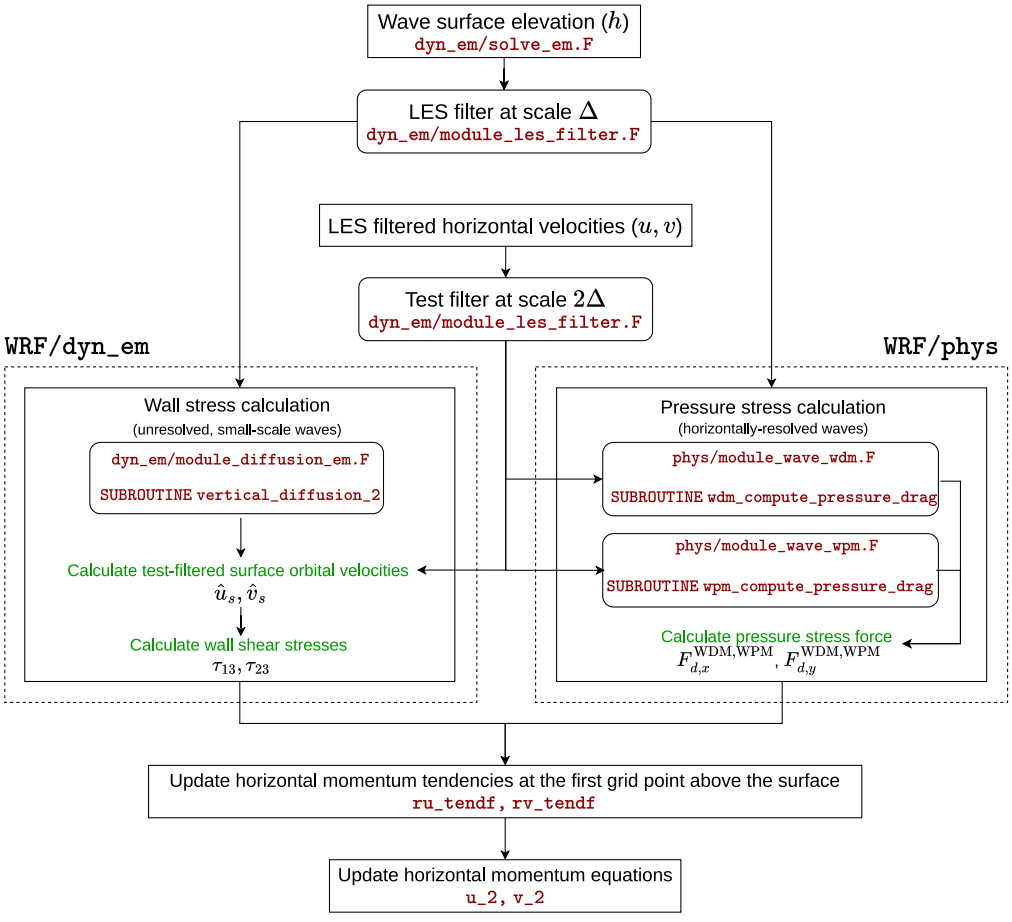

Figure 1. A simple flowchart representing the implementation of wave-phase-aware models in the WRF-LES framework.

A schematic flowchart illustrating the implementation of the wave-phase-aware models within the WRF-LES framework is presented in Figure 1. First, the wave surface elevation is computed in `dyn_em/solve_em.F`. The resulting surface elevation is then filtered at the LES filter scale, Δ, and passed to the relevant subroutines in the `dyn_em` and `phys` components of the WRF model.

https://doi.org/10.5194/egusphere-2026-2292
Preprint. Discussion started: 2 June 2026

The stress contribution from unresolved waves in the WDM and WPM is computed within the WRF dynamical core in `dyn_em/module_diffusion_em.F`, specifically through the `vertical_diffusion_2` subroutine. In this step, the test-filtered surface orbital velocities are evaluated in the diffusion package of WRF-LES, and the corresponding horizontal momentum tendencies are updated using the boundary conditions given by Equation (29). Note that the vertical surface orbital velocity is set to zero in the wave-phase-aware models. A similar procedure is applied for the MOW model; however, no test filtering is performed, and the vertical surface orbital velocity is non-zero, as defined in Equation (29).

The pressure stress is computed within the `phys` package of the corresponding wave-phase-aware model, after which the horizontal momentum tendencies at the first grid point above the surface are updated using the calculated pressure stress forces. Finally, the horizontal momentum equations are updated to incorporate both unresolved and resolved wave stresses within the filtered WRF-LES momentum equations.

All wave models presented in this manuscript are configured for idealized channel flow simulations. Accordingly, the surface layer schemes must be disabled (`sf_sfclay_physics` $= 0$). In addition, `isfflx` $= 0$ should be specified to apply a quadratic drag law for the computation of momentum fluxes. Namelist options for the wave-phase-aware models are summarized in Table A1.

3.1 Modifications to wave stress modeling in wave-phase-aware models

To enable consistent comparison across modeling approaches, a unified wall stress formulation is adopted in all simulations. The wave-phase-aware models (WDM and WPM) are modified to match the MOW formulation in terms of drag law, velocity input location, and filtering procedure, thereby removing discrepancies in the representation of unresolved wave stress. This approach ensures that differences in model behavior arise primarily from the treatment of resolved wave dynamics.

It is important to note that, although Aiyer et al. (2023) does not explicitly state that the model accounts for a reversal of momentum transfer from the waves to the airflow when $\mathbf{u}-c<0$, the original implementation implicitly incorporates this effect through a local `sgn` function, i.e., `sgn`$(\mathbf{u}-c)$. This term is not included in the original formulation given in Equation (13), but its role is clarified in a later extension of the wave drag model (Aiyer et al., 2024). To ensure a consistent and explicit representation of the momentum transfer direction, we introduce an additional directional factor, using $\nabla h/|\nabla h|$, following the framework of Ayala et al. (2024). Importantly, this modification does not alter the underlying physics of the original model, as the added term is a unit vector that solely prescribes direction. Rather, it provides a more rigorous and unified formulation by aligning the directional treatment with $\nabla h/|\nabla h|$ across both wave-phase-aware models. The instantaneous drag force per unit area is then formulated as

$$F_{d,i}^{\mathrm{WDM}} = -C_D \frac{\rho}{\Delta z} u_i U^{\Delta} \left(n_k \cdot \frac{\partial h}{\partial x_k} \right) H \left(n_k \cdot \frac{\partial h}{\partial x_k} \right) \frac{\nabla h}{|\nabla h|}, \qquad \text{for } i,k = 1,2. \tag{24}$$

Our analysis of the pressure drag predicted by the WDM shows that the model slightly overestimates the magnitude of pressure drag for wave ages $c/u_* \leq 10$ compared to the results from the MOW model. However, substantially larger discrepancies arise for $c/u_* > 10$ when compared with the wave-phase-resolved MOW results. In particular, the WDM fails to capture the decay of pressure drag with increasing wave age and predicts larger magnitudes of negative pressure drag than those obtained from

https://doi.org/10.5194/egusphere-2026-2292
Preprint. Discussion started: 2 June 2026

the MOW simulations. As a result, the model imposes excessive negative drag on the mean flow, leading to an unrealistically strong increase in the mean velocity profile. These results indicate a clear dependence of pressure drag on wave age that is not accounted for in the original WDM formulation, especially in the transitional and fast wave regimes. Previous studies have reported that pressure drag decreases approximately exponentially with increasing wave age for $c/u_* \gtrsim 6$ for monochromatic waves (Yang and Shen, 2010; Liu et al., 2010; Ayala et al., 2024). Motivated by this behavior, we fit an exponential function to the pressure drag obtained from the MOW simulations and incorporate the wave age dependence into the WDM through a modification of the drag coefficient, C_D, given by Equation (14). This correction also slightly reduces the drag predicted by the model for slow waves. With the proposed correction, the WDM results show significantly improved agreement with the MOW simulations and closely follow the WPM predictions with only negligible differences in the transitional regime up to $c/u_* = 24$. The results of this analysis are presented in Section 6.2.

The modified instantaneous drag force per unit area that accounts for wave age variation in its drag coefficient is then formulated as

$$F_{d,i}^{\mathrm{WDM^{mod}}} = -C_D^{\mathrm{mod}} \frac{\rho}{\Delta z} u_i U^{\Delta} \left(n_k \cdot \frac{\partial h}{\partial x_k} \right) H \left(n_k \cdot \frac{\partial h}{\partial x_k} \right) \frac{\nabla h}{|\nabla h|}, \qquad \text{for } i,k = 1,2, \tag{25}$$

with the proposed modified drag coefficient, $C_D^{\mathrm{mod}} = C_D \times f(c/u_*)$,

$$C_D^{\mathrm{mod}} = \left[\frac{P}{1 + Q(ak)^2} ak \right] \exp\left(- \left[\frac{c/u_*}{(c/u_*)_{\mathrm{threshold}}} \right]^{\alpha} \right), \tag{26}$$

with $(c/u_*)_{\mathrm{threshold}} = 10$, and $\alpha = 1.4$.

4 Setup of turbulent flow over monochromatic waves under idealized conditions

To evaluate the performance of the wave-phase-aware models of Aiyer et al. (2023) (WDM) and Ayala et al. (2024) (WPM) against the higher-fidelity, wave-phase-resolved approach of Zhu et al. (2023) (MOW), we simulate turbulent flow over a sinusoidal wave train within a unified LES framework. Here, both the mean wind and the wave field are assumed to be aligned in the streamwise x-direction. We analyze the mean momentum budget and wind speed profiles across a wide range of wave steepnesses and wave ages. A detailed description of the simulated wave regimes is provided in Section 4.1.

The wave surface elevation is prescribed as a sinusoidal function,

$$h(x,y,t) = a\cos\gamma, \tag{27}$$

where

$$\gamma = k\left(x\cos\theta_0 + y\sin\theta_0 - ct\right) + \phi. \tag{28}$$

Here, a is the wave amplitude, $k = 2\pi/\lambda$ is the wavenumber with λ the wavelength, (x,y) denote the streamwise and spanwise coordinates, θ_0 is the wave propagation direction, $c = \sqrt{g/k}$ is the wave phase velocity, t is time, and ϕ is the phase angle. The

https://doi.org/10.5194/egusphere-2026-2292
Preprint. Discussion started: 2 June 2026

corresponding wave-induced orbital velocities are given by

$$u_s = a\omega \cos\gamma \cos\theta_0, \tag{29a}$$

$$v_s = a\omega \cos\gamma \sin\theta_0, \tag{29b}$$

$$w_s = a\omega \sin\gamma, \tag{29c}$$

where $\omega = \sqrt{gk}$ is the wave angular frequency and $g = 9.81\ \mathrm{ms}^{-2}$ is the gravitational acceleration. In our simulations, the surface boundary condition accounts only for the prescribed wave surface orbital velocities and the mean wind in the streamwise direction; no additional mean surface current or drift velocity is imposed at the lower boundary.

4.1 Description of the simulated wave regimes

The first objective of this study is to implement the two wave-phase-aware models described in Section 3 and to verify the implementation of the Wave Drag Model (WDM). The Windward Potential Flow Model (WPM) is implemented but not formally verified due to differences between its original validation setup and the present WRF-LES framework. The second objective is to evaluate the performance of these models across a wide range of wind and wave conditions within a consistent WRF-LES framework, using the moving-wave (MOW) model as a reference. The MOW model is used in its original, previously validated form (Zhu et al., 2023) and is therefore not re-verified in this study.

To verify the WDM implementation of Aiyer et al. (2023) within WRF-LES, four simulations were conducted with varying grid resolutions across three representative wave regimes. The results were compared against reference simulations obtained from an independent implementation of WDM in the pseudo-spectral LES code LESGO developed at Johns Hopkins University. While the original formulation of WDM in Aiyer et al. (2023) was developed and tested using the NGA solver (Desjardins et al., 2008; MacArt and Mueller, 2016), the LESGO implementation follows the same formulation and serves as a consistent reference for verification. For this initial verification, WDM is used in its original form, without incorporating the modifications to the unresolved stress parameterization or the pressure drag treatment proposed in the present study.

For the case with wave regime $c/u_* = 11$ and $ak = 0.27$ from Husain et al. (2022), a coarse grid resolution was employed, while for the case $c/u_* = 20$ and $ak = 0.15$, a fine grid resolution was used to assess the sensitivity of mean flow and second-order turbulence statistics to grid resolution. In addition, both coarse and fine resolutions were tested for the intermediate regime $c/u_* = 18$ and $ak = 0.10$ from Aiyer et al. (2024), with results again compared to LESGO. The full set of simulation parameters is summarized in Table 1.

No additional verification of the WPM of Ayala et al. (2024) is performed in this work. The original validation was conducted at relatively low Reynolds numbers requiring very fine grid resolutions typical of canonical incompressible LES. Such conditions are not directly compatible with the higher-Reynolds-number, compressible WRF-LES framework employed here, and reproducing those cases would require prohibitively fine spatiotemporal resolution beyond the scope of this study. Accordingly, WPM is evaluated here through comparison against the MOW reference within a consistent WRF-LES configuration, rather than through direct reproduction of the original validation cases.

https://doi.org/10.5194/egusphere-2026-2292
Preprint. Discussion started: 2 June 2026

Table 1. Simulated wave regimes and parameters for WDM verification analysis.

Model	Parameter	Unit	Case 1	Case 2		Case 3
			Coarse	Coarse	Fine	Fine
WDM	c/u_*	[−]	11	18	18	20
	ak	[−]	0.27	0.10	0.10	0.15
	u_*	[$\mathrm{m\,s^{-1}}$]	0.490	0.443	0.443	0.443
	$\Delta x = \Delta y$	[m]	2	3.25	1.6	3
	Δz	[m]	~ 2	~ 1.6	~ 1.6	~ 3
	$N_x \times N_y \times N_z$	[−]	$48 \times 48 \times 25$	$64 \times 64 \times 48$	$128 \times 128 \times 48$	$86 \times 86 \times 54$
	$L_x = L_y$	[m]	5λ	5λ	5λ	5λ
	L_z	[m]	2.5λ	2λ	2λ	3λ
	λ	[m]	19	41	41	51
	Δt	[s]	1/75	1/100	1/200	1/100
	t_{eddy}	[s]	L_z/u_*	L_z/u_*	L_z/u_*	L_z/u_*
	t_{sim}	[s]	$100t_{\mathrm{eddy}}$	$100t_{\mathrm{eddy}}$	$100t_{\mathrm{eddy}}$	$100t_{\mathrm{eddy}}$
	SFS model	[−]	Smagorinsky	Smagorinsky	Smagorinsky	Smagorinsky
	C_{Smag}	[−]	0.16	0.16	0.16	0.16

Finally, the performance of the wave-phase-aware models is assessed relative to the higher-fidelity wave-phase-resolved MOW model across a broad range of wave conditions under neutral channel flow. Previous studies have explored different regions of the wave parameter space: Aiyer et al. (2023) considered wave ages $1.4 \leq c/u_* \leq 16.2$ with steepness $0.06 \leq ak \leq 0.27$, while Ayala et al. (2024) extended this range to wave ages up to $c/u \approx 54.3$ with $0.10 \leq ak \leq 0.26$. In contrast, Zhu et al. (2023) performed wave-phase-resolved simulations at three discrete wave ages ($c/u_* = 15, 28$, and 50) for a single steepness of $ak = 0.10$. By situating the present analysis across these complementary parameter ranges, we provide a comprehensive assessment of the capabilities and limitations of each modeling approach under overlapping conditions.

In this study, we consider a range of wave conditions defined by combinations of wave ages $c/u_* = 8, 10, 17, 21, 24$ and wave steepness values $ak = 0.10, 0.18, 0.25$, resulting in a total of 15 simulations for each model. Table 2 summarizes the total of 45 wall-modeled LESs for a wide range of wave regimes.

5 WRF-LES configuration for wave-phase-resolved and for wave-phase-aware wave modeling

In all simulations, we use a constant pressure gradient in the streamwise direction to drive the wind flow over monochromatic waves, given by

$$-\frac{1}{\rho}\frac{\partial P}{\partial x} = \frac{u_*^2}{H}, \tag{30}$$

https://doi.org/10.5194/egusphere-2026-2292
Preprint. Discussion started: 2 June 2026

Table 2. Simulated wave regimes and parameters for evaluating wave-phase-aware models against MOW.

Models	c/u_* [−]	ak [−]	u_* [$\mathrm{m\,s^{-1}}$]	λ [m]	$z_{0,b}$ [m]	$kz_{0,b}$ [−]
	8		0.800			
1) MOW	10		0.640			
2) WDM	17	0.10, 0.18, 0.25	0.376	26.25	2×10^{-3}	4.8×10^{-4}
3) WPM	21		0.305			
	24		0.266			

Note. Here, c/u_* denotes the wave age and ak represents the wave steepness, where u_* is the friction velocity, λ is the wavelength, and $z_{0,b}$ is the background surface roughness length. Each combination of wave age and wave steepness is driven by a constant pressure gradient in the streamwise direction, with its magnitude set consistently with the specified friction velocity. In all simulations, the wave phase velocity c, together with the wavelength (and thus the wavenumber), is held constant. Wave steepness is varied by adjusting the wave amplitude a, which alters the ratio ak while keeping other parameters fixed.

with H being the domain height. This approach is consistent with idealized LES setups, where prescribing a constant pressure gradient allows control of the surface friction velocity and maintains the desired mean flow (Zhu et al., 2023; Aiyer et al., 2023; Ayala et al., 2024). The modified version of WRF v3.8.1 requires $\partial P/\partial x$ as an input, and thus we use an air density of $\rho = 1.1673\ \mathrm{kg\,m^{-3}}$ to calculate the pressure gradient. Although WRF is a compressible flow model and ρ varies slightly during the simulation, under neutral channel flow conditions, air density can be reasonably assumed constant. For each wave regime, the surface friction velocity u_* is prescribed from Table 2. For all wave steepnesses considered here, we set the wave amplitude to $a = 0.418$ m for $ak = 0.10$, $a = 0.752$ m for $ak = 0.18$, and $a = 1.045$ m for $ak = 0.25$, with a constant wavelength of $\lambda = 26.25$ m.

The computational domain for all simulations is $160\ \mathrm{m} \times 160\ \mathrm{m} \times 52.5\ \mathrm{m}$, corresponding to $L_x = L_y = 6\lambda$ and $L_z = H = 2\lambda$, such that six waves are present in the horizontal plane and the wavelength is resolved by at least 10 grid points in both x and y. The wave-phase-aware models are discretized with a grid of $64 \times 64 \times 22$ points, whereas the wave-phase-resolved model uses $64 \times 64 \times 32$ grid points. Because the wave-phase-resolved implementation explicitly resolves the vertical structure of the wave surface, it requires more vertical grid points and is therefore more computationally expensive. Horizontal grid spacings are held constant in all simulations with $\Delta x = \Delta y = 2.5$ m. Near the surface, the vertical grid spacing is $\Delta z \approx 0.18$ m for the wave-phase-resolved case, while it is $\Delta z \approx 2.5$ m for the wave-phase-aware cases, yielding a grid aspect ratio of $\Delta x/\Delta z = \Delta y/\Delta z \approx 1$ in wave-phase-aware simulations. Above this, the vertical grid is continuously stretched by a factor of 1.05 up to the top of the domain. All simulations are integrated until the flow reaches a statistically steady state, which occurs after approximately 200-300 τ_e, where $\tau_e = H/u_*$ is the eddy turnover time associated with the surface friction velocity. Model results are averaged over the final 40-50 eddy turnover times to compute statistically converged flow statistics.

The domain top is treated with zero vertical velocity and zero stress, without damping or a capping inversion, to prevent the upper boundary from affecting the near-surface flow. In all simulations, small perturbations drawn from a pseudo-random

https://doi.org/10.5194/egusphere-2026-2292
Preprint. Discussion started: 2 June 2026

uniform distribution in the range $[-0.2, +0.2]\ \mathrm{m\,s^{-1}}$ are added to the initial streamwise velocity field to seed turbulence. The Smagorinsky closure scheme is employed to represent subfilter-scale turbulence, with a constant Smagorinsky coefficient of $C_S = 0.16$ used to compute the turbulent eddy viscosity.

The discretization in the vertical direction, N_z, is chosen to ensure that the waves lie below the cell center of the first grid point, following the criterion $a < 0.95\,\Delta z/2$ used in previous wave drag LES studies (Aiyer et al., 2023). Here, we apply a more stringent criterion of $a < 0.85\,\Delta z/2$ for the wave-phase-aware simulations to ensure that the prescribed monochromatic waves always lie below the cell center of the first grid point off the wall, given that Δz in WRF can vary slightly in time due to pressure variations at each grid point.

The time step size, Δt, for the wave-phase-resolved simulations is held constant at $\Delta t = 0.01$ s, whereas the wave-phase-aware models employ varying values of Δt ranging from 0.02 s down to 0.005 s to ensure numerical stability. The requirement for smaller time steps in wave-phase-aware simulations stems from the more restrictive stability constraints associated with explicit finite difference schemes such as those used in WRF-LES. In the wave-phase-aware framework, particularly in the WDM implementation, strong, localized pressure drag forces applied near the surface can substantially enhance near-surface momentum exchange. These large drag perturbations effectively increase the characteristic advective and wave-related speeds experienced by the numerical scheme, thereby tightening the stability limits on the allowable time step.

Although such simulations may proceed without triggering explicit CFL error messages, numerical instabilities can still arise when the time step is too large. These instabilities typically manifest as unphysical velocity fields or the generation of undefined floating-point values (NaNs). This behavior arises because the extreme, localized drag forcing at the first LES grid level introduces numerical stiffness that is not fully captured by the standard CFL criterion, which primarily constrains advective stability. When the drag magnitude becomes particularly large, such as in low wave age regimes, the explicit time integration may become unstable despite formally satisfying the CFL condition, leading to rapid, nonphysical velocity growth. Reducing Δt, and in some cases applying additional damping to suppress unresolved high-frequency fluctuations, mitigates this stiffness and restores numerical stability.

These stability issues are most pronounced in low wave age regimes (e.g., $c/u_* \lesssim 6$), where the wave-induced drag forcing becomes particularly strong. Consequently, such conditions were not considered in the present analysis, which instead focuses on moderate to high wave ages ($c/u_* \geq 8$), for which stable time integration can be achieved.

6 Results

This section begins with a verification analysis of the original WDM formulation of Aiyer et al. (2023), using the wave regimes summarized in Table 1. The modified WDM and WPM formulations described in Section 3.1 are then evaluated over a different set of wave regimes listed in Table 2, using the MOW model as a reference. In the remainder of this manuscript, $\langle\cdot\rangle$ denotes spatial averaging in the horizontal directions.

https://doi.org/10.5194/egusphere-2026-2292
Preprint. Discussion started: 2 June 2026

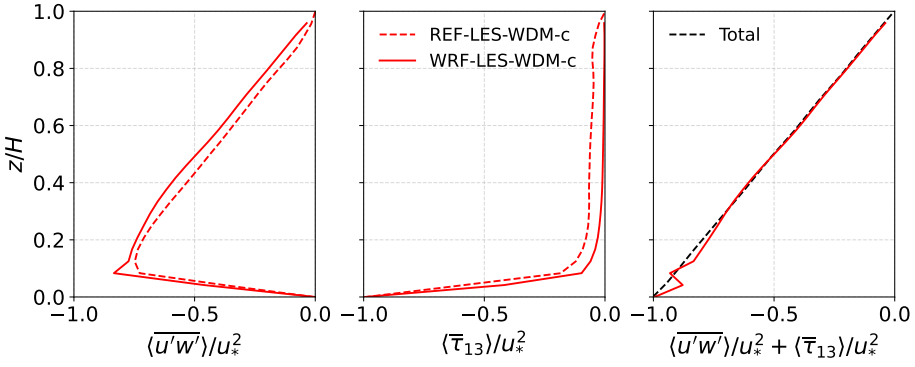

(a) Case 1 ($c/u_* = 11, ak = 0.27$).

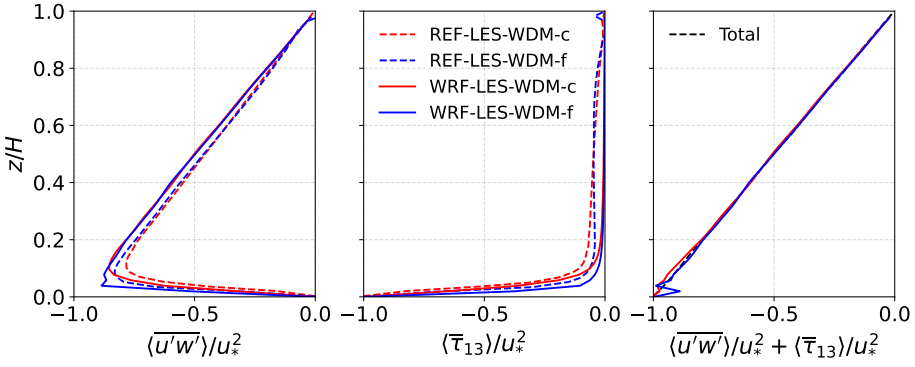

(b) Case 2 ($c/u_* = 18, ak = 0.10$).

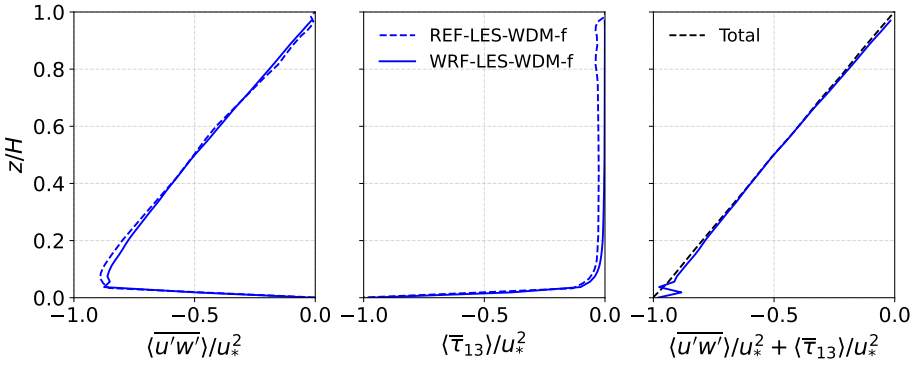

(c) Case 3 ($c/u_* = 20, ak = 0.15$).

Figure 2. Normalized temporally and laterally averaged profiles of resolved (first panel), subfilter-scale (middle panel), and total (last panel) shear stress are shown for $c/u_* = 11, ak = 0.27$ from Husain et al. (2022) (a), $c/u_* = 18, ak = 0.10$ from Aiyer et al. (2024) (b), and $c/u_* = 20, ak = 0.15$ (c). Results from WRF-LES-WDM (solid lines) and LESGO-WDM (dashed lines) are compared across different grid resolutions.

https://doi.org/10.5194/egusphere-2026-2292
Preprint. Discussion started: 2 June 2026

6.1 Verification of the Wave Drag Model (WDM) implementation in WRF-LES

In Figure 2, we present time-averaged and laterally averaged normalized vertical profiles of resolved shear stress, subfilter-scale stress (including the pressure stress predicted by WDM at the surface), and total shear stress for three different wave regimes at varying spatial grid resolutions. In all cases, WRF-LES-WDM reproduces the near-surface shear stresses well, with slight deviations appearing beyond $z/H \approx 0.15$, which are likely attributable to differences in the numerical schemes employed by the two LES codes. Specifically, LESGO uses a pseudo-spectral method in the horizontal directions, while the vertical direction is discretized using a second-order central finite difference scheme. In contrast, the WRF-LES model uses fifth- and third-order finite difference schemes for horizontal and vertical advection, respectively.

Figure 3 shows the temporally and horizontally averaged normalized velocity profiles along the channel height for the considered wave regimes. In the slow wave case (Figure 3a), both the present implementation and the reference data exhibit identical velocity magnitudes at the surface, indicating that the WDM is accurately implemented within the WRF-LES framework. For the moderate (Figure 3b) and fast (Figure 3c) wave cases, the WRF-LES model slightly underestimates the near-surface velocity magnitude compared to the reference data by approximately $\sim 2\%$ and $\sim 3\%$, respectively. However, these differences are negligible.

It should be noted that differences in the velocity profiles within the logarithmic region arise from a combination of numerical and modeling factors, including differences in discretization schemes, implicit filtering, and the effective implementation of the SFS model. Although both simulations employ the same Smagorinsky formulation with identical C_{Smag} coefficient, differences in numerical dissipation influence the partitioning between resolved and SFS stresses, leading to deviations in the mean velocity profiles. While the near-wall grid spacing is comparable between the two configurations, the use of vertical grid stretching in

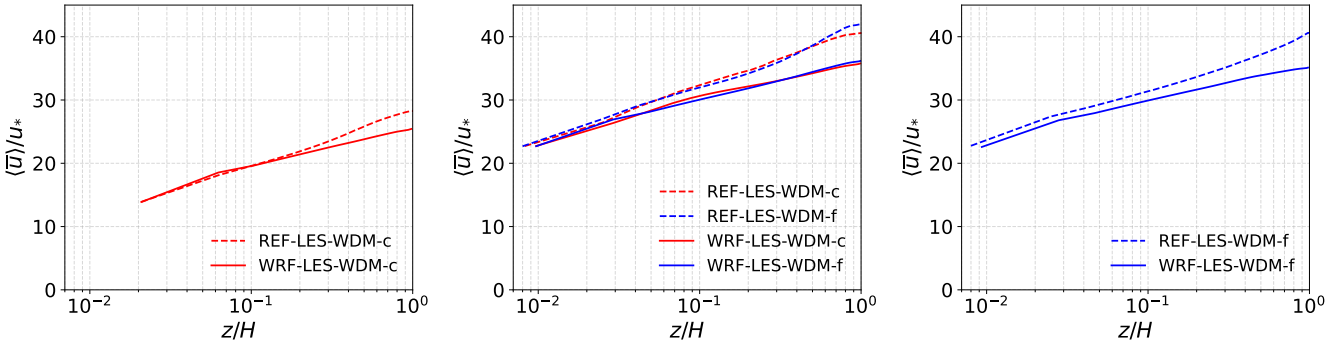

(a) Case 1 ($c/u_* = 11, ak = 0.27$). (b) Case 2 ($c/u_* = 18, ak = 0.10$). (c) Case 3 ($c/u_* = 20, ak = 0.15$).

Figure 3. Normalized mean streamwise velocity profiles for $c/u_* = 11, ak = 0.27$ from Husain et al. (2022) (a), $c/u_* = 18, ak = 0.10$ from Aiyer et al. (2024) (b), and $c/u_* = 20, ak = 0.15$ (c) for the WRF-LES-WDM (solid lines) and LESGO-WDM (dashed lines) for varying grid resolutions.

https://doi.org/10.5194/egusphere-2026-2292
Preprint. Discussion started: 2 June 2026

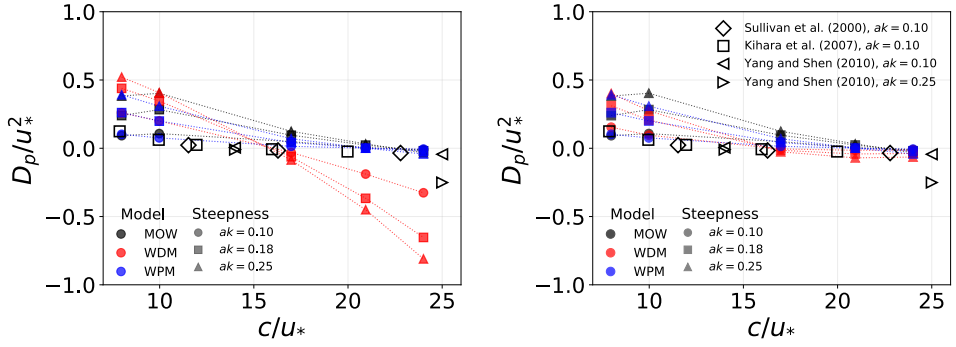

(a) Original WDM (Equation (24)).

(b) Modified WDM (Equation (25)).

Figure 4. Normalized form stress as a function of wave age for $c/u_* = 8, 10, 17, 21$, and 24 and $ak = 0.10, 0.18$, and 0.25 for the original WDM (Equation (24)) and modified WDM formulation (Equation (25)). Colors indicate different models, filled symbols correspond to wave steepness levels, and open symbols denote DNS data from Sullivan et al. (2000), Kihara et al. (2007), and Yang and Shen (2010).

WRF-LES, compared to the uniformly distributed vertical grid in LESGO, can still influence the representation of turbulence and stress distribution away from the wall, contributing to differences in the log-layer structure.

6.2 Intercomparison of wave-coupled models and implications for WDM corrections

In this section, we compare wave-phase-aware and wave-phase-resolved models and examine the resulting implications for modifications to the Wave Drag Model (WDM) of Aiyer et al. (2023), adopting a normalized background surface roughness length of $kz_{0,b} \approx 4.8 \times 10^{-4}$.

In the wave-phase-resolved simulations, the wave-induced pressure stress at the surface is obtained directly from the resolved pressure field through the correlation between the surface pressure and the local wave slope, as

$$D_p^{\mathrm{MOW}} = \frac{1}{\lambda} \int_0^{\lambda} \frac{\tilde{p}}{\rho} \frac{\partial z}{\partial \xi}\bigg|_{\zeta=1} dx. \tag{31}$$

On the other hand, for the wave-phase-aware models, Equation (31) cannot be used to determine the pressure drag from the resolved pressure field, since the waves are not explicitly resolved in the vertical direction. Instead, for the WDM and WPM models, the pressure stress is computed through a drag force per unit volume formulation given by

$$D_p^{\mathrm{WDM}} = C_D^{\mathrm{mod}} \mathbf{u} U^{\Delta} \left(n_k \cdot \frac{\partial h}{\partial x_k} \right) H \left(n_k \cdot \frac{\partial h}{\partial x_k} \right) \frac{\nabla h}{|\nabla h|}, \tag{32}$$

$$D_p^{\mathrm{WPM}} = \frac{1}{\pi} \left| (\mathbf{u} - \mathbf{C}) \cdot \frac{\nabla h}{|\nabla h|} \right|^2 |\nabla h|^2 H \left((\mathbf{u} - \mathbf{C}) \cdot \nabla h \right) \frac{\nabla h}{|\nabla h|}. \tag{33}$$

In Figure 4a, the normalized pressure drag predictions as a function of wave age from WPM and MOW show good agreement across all wave steepness levels. In particular, for $ak = 0.10$, both models closely follow the trends observed in DNS

https://doi.org/10.5194/egusphere-2026-2292
Preprint. Discussion started: 2 June 2026

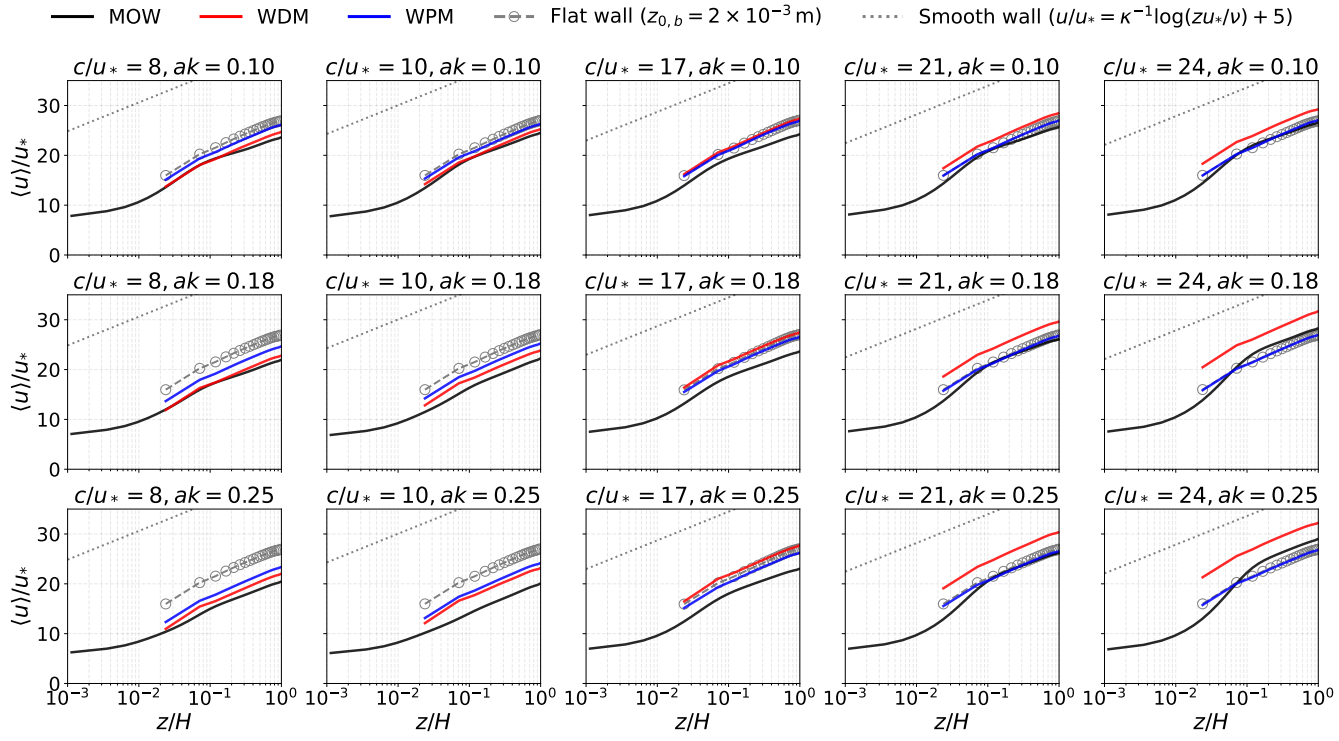

Figure 5. Normalized mean streamwise velocity profiles for $c/u_* = 8, 10, 17, 21, 24$ and $ak = 0.10, 0.18, 0.25$ for all models using the original WDM formulation (Equation (24)). Velocity profiles from the flat wall simulations without waves using a background surface roughness length of $z_{0,b} = 2 \times 10^{-3}$ m are also given as reference (gray lines with markers). Dotted gray lines indicate the theoretical velocity profiles for smooth walls.

data from the literature. In contrast, WDM slightly overestimates the pressure drag in the slow wave regime ($c/u_* = 8$-10) by a factor of approximately 1.5-2, with the discrepancy increasing as the wave age increases. While MOW and WPM exhibit near-zero pressure drag, including negative values at $c/u_* = 24$, the WDM results indicate an almost negligible contribution from unresolved wave stress to the total stress. This behavior is reflected in the normalized resolved wave stress (i.e., pressure drag), which attains a value of approximately -0.95 for $ak = 0.25$. As wave age increases ($c/u_* \geq 17$), WDM predicts progressively more negative pressure drag, and this systematic overestimation leads to an overprediction of the velocity magnitude, as evidenced by the velocity profiles shown in Figure 5.

Based on this analysis and insights from the literature, we propose improving the WDM formulation by introducing a simple correction that reduces the magnitude of the imposed pressure drag. Specifically, the drag coefficient is modified to depend on both wave steepness and wave age, decreasing with increasing wave age. After applying the drag coefficient modification to the original WDM, as described in Equation (25), the predicted pressure drag (Figure 4b) and velocity profiles (Figure 6) are

https://doi.org/10.5194/egusphere-2026-2292
Preprint. Discussion started: 2 June 2026

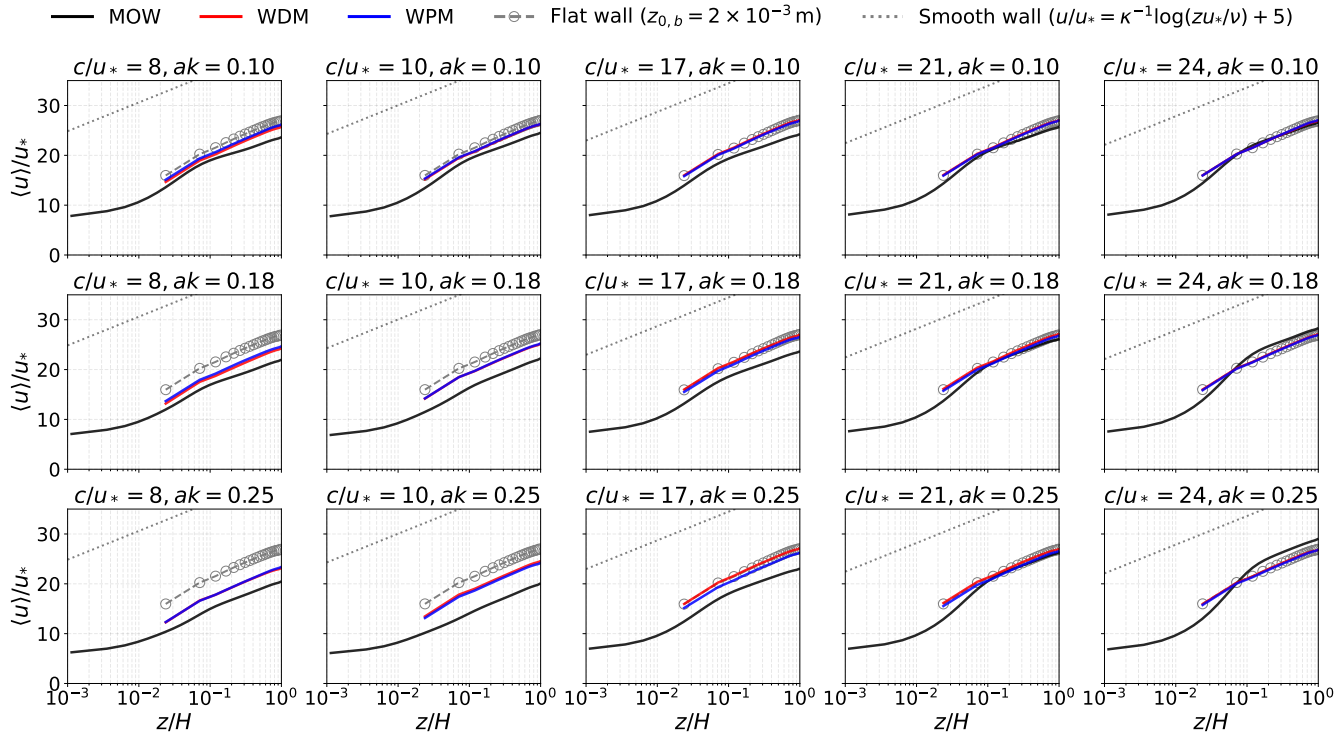

Figure 6. Same as Figure 5, but for modified WDM (Equation (25)).

significantly improved and show close agreement with WPM and MOW results, as well as with DNS pressure drag data for $ak = 0.10$ from the literature.

We observe that both the MOW results and DNS data from the literature exhibit an exponential decrease with increasing wave age. Motivated by this behavior, we propose a simple exponential correction that decreases with wave age. This correction is incorporated into the original drag coefficient, C_D, as given in Equation (26). Specifically, the pressure drag predicted by the original WDM formulation is multiplied by this exponential function and compared against the MOW and DNS data. Since modifying C_D directly affects the predicted pressure drag and, consequently, the local velocity field, the impact of this correction is evaluated accordingly. While the WDM already overestimates pressure drag in the slow wave regime, the proposed correction introduces a slight reduction in this region to better align with high-fidelity data. More importantly, it significantly reduces the pressure drag in the transitional regime for $c/u_* \geq 10$ up to $c/u_* \approx 25$, where the original model exhibits the largest discrepancies. The exponent $\alpha = 1.4$ in the proposed correction is determined through a trial-and-error procedure, as the mean velocity profiles are sensitive to the imposed pressure drag during the simulations. Future work could explore alternative functional forms for the drag coefficient to better capture its dependence on wave and flow parameters.

Additionally, we examine how models of different fidelity modify the wave-induced streamwise velocity under slow ($c/u_* = 8$), moderate ($c/u_* = 17$), and fast ($c/u_* = 24$) wave conditions at a steepness of $ak = 0.25$. To this end, the velocity field is

https://doi.org/10.5194/egusphere-2026-2292
Preprint. Discussion started: 2 June 2026

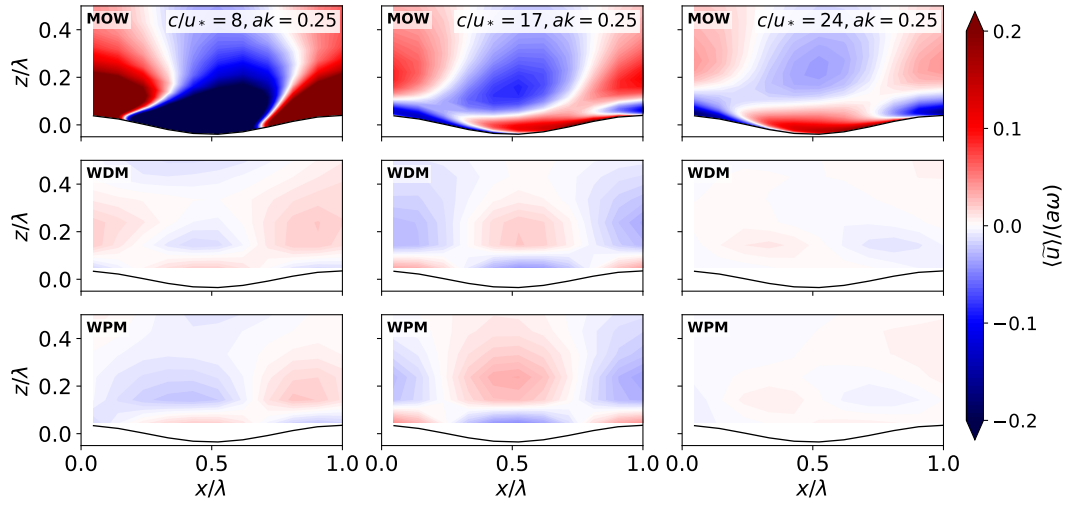

Figure 7. Contours of the normalized wave-induced streamwise velocity, $\langle\tilde{u}\rangle/(a\omega)$, where a is the wave amplitude and ω is the wave frequency, in the x-z plane for the MOW (first row), WDM (second row), and WPM (third row) models at $c/u_* = 8, 17$, and 24 with $ak = 0.25$.

decomposed into mean, wave-coherent, and turbulent components using the triple decomposition framework of Hara and Sullivan (2015). An instantaneous quantity is decomposed as

$$f = \langle f \rangle + \widetilde{f} + f', \tag{34}$$

where $\langle f \rangle$ is the mean component, $\widetilde{f}$ is the wave-coherent fluctuation obtained via phase averaging, and f' represents turbulent fluctuations. The phase average is computed by aligning flow realizations with a common wave phase and averaging in space and time, after which the remaining fluctuations define the turbulent component.

Figure 7 shows contour maps of the normalized wave-induced streamwise velocity in the x-z plane for the wave-phase-resolved (MOW) model at wave ages $c/u_* = 8, 17, 24$ and steepness $ak = 0.25$. As the wave age increases, the near-surface wave-induced velocity contours develop a pronounced upstream tilt across all models and steepness conditions. However, the magnitudes predicted by the wave-phase-aware models are at least one order of magnitude smaller than those from the wave-phase-resolved MOW simulations (see Figure 8).

The normalized wave-induced streamwise velocity fields from the wave-phase-aware models in Figure 8 exhibit similar behavior for $c/u_* \geq 17$. In the slow wave regime, however, WPM predicts stronger negative velocity regions near the first crest compared to both WDM and MOW (see the first panel of Figure 7). At the same time, the vertical extent of the negative velocity in the trough is qualitatively closer to the MOW results than to the WDM predictions. For $c/u_* = 24$, both wave-phase-aware models reproduce the overall spatial pattern observed in the MOW simulations, albeit with velocity magnitudes that are approximately one order of magnitude smaller.

https://doi.org/10.5194/egusphere-2026-2292
Preprint. Discussion started: 2 June 2026

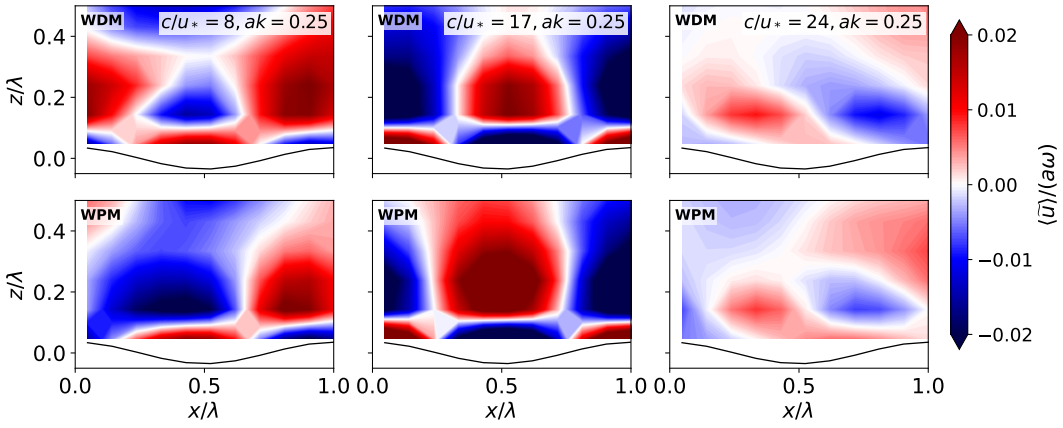

Figure 8. Same as Figure 7, but for the wave-phase-aware models only, with a rescaled colorbar range. The first row corresponds to WDM and the second row to WPM. Note that the color scale differs from the results shown in Figure 7, as the normalized wave-induced velocity magnitudes are approximately one order of magnitude smaller.

7 Conclusions and discussion

In this study, we implemented the wave drag model (WDM) of Aiyer et al. (2023) and the Windward Potential Flow Model (WPM) of Ayala et al. (2024) within the WRF-LES v3.8.1 framework. This unified implementation enables direct comparison between these wave-phase-aware models and the wave-phase-resolved moving-wave model (MOW) of Zhu et al. (2023), which has previously been incorporated into the same codebase. Although wave-phase-aware models exist in the literature, they are typically implemented in different LES solvers, complicating model intercomparison due to variations in numerical schemes. By integrating all models within a consistent framework, this work isolates physical model differences from numerical artifacts. The resulting wave-phase-aware model implementations in WRF-LES v3.8.1 are made openly available, providing a transparent and extensible framework to support reproducibility and facilitate future model development by the community.

To ensure consistency, we modified the unresolved wave stress formulations of the wave-phase-aware models so that they follow the same stress modeling framework used in the wave-phase-resolved MOW implementation in WRF-LES. In addition, we introduced an explicit directional term in the WDM pressure drag formulation (Equation (24)) to account for the sign of momentum transfer. While this effect is implicitly represented in the original implementation through a local `sgn` function, it is not included in the published formulation of Aiyer et al. (2023) (see Equation (13)). Following Ayala et al. (2024), we standardized the directional representation by incorporating the unit vector $\nabla h/|\nabla h|$, thereby providing a consistent and physically interpretable formulation without altering the underlying original model physics.

Furthermore, we propose a simple correction to the WDM formulation by introducing an exponential decay function in the drag coefficient, C_D, as a function of wave age (Equation (26)). This modification mitigates the excessive pressure drag predicted by WDM in the transitional regime and slightly reduces the imposed drag in the slow wave regime, in agreement with the pressure drag behavior obtained from the MOW model. Note that the proposed correction improves the WDM predictions

https://doi.org/10.5194/egusphere-2026-2292
Preprint. Discussion started: 2 June 2026

for wave ages up to approximately $c/u_* \approx 25$. For larger wave ages ($c/u_* \gtrsim$ 25-30), the modified drag coefficient approaches near-zero values, and available literature data for validation become scarce. Therefore, for swell-dominated regimes, we recommend employing the additional correction proposed by Aiyer et al. (2024), which is based on a linear fit to wall-resolved LES data from Cao and Shen (2021).

The stress profiles predicted by WDM from LESGO and the present WRF-LES implementation in the verification analysis, including Reynolds stress, subfilter-scale stress, and total stress, show very similar behavior across the two LES codes, with minor differences appearing above $z/H \approx 0.1$. In addition to this, although the velocity profiles exhibit slight deviations in the logarithmic region across all three cases, the WDM-modified velocity at the first grid point shows no difference for $c/u_* = 11$, $ak = 0.27$, while a difference of approximately 3% is observed for $c/u_* = 20$, $ak = 0.15$.

The velocity profiles predicted by the WDM and WPM models across the additional wave regimes considered in this study remain in close agreement with each other, indicating that both wave-phase-aware models produce comparable resolved wave pressure drag. For intermediate wave age ($c/u_* = 21$), the mean velocity profiles agree closely with the MOW results, with relative deviations ranging from 11.9% to 25.2% across all wave steepness values ($ak = 0.10, 0.18, 0.25$). At the higher wave age of $c/u_* = 24$, the agreement remains strong for the low-steepness case ($ak = 0.10$), with deviations of approximately 11%. For steeper waves, discrepancies reach up to 15.5% and 22.4% at the first grid point for $ak = 0.18$ and 0.25, respectively. In these cases, both WDM and WPM slightly underestimate the mean velocity in the logarithmic region relative to MOW. In contrast, for lower wave ages ($c/u_* = 8$ and 10), the wave-phase-aware models show smaller discrepancies in the near-surface mean velocity, ranging from approximately 7.9% to 18.1% across $ak =$ 0.10-0.25.

Overall, the agreement between the wave-phase-aware models and MOW remains good across all wave regimes, although the deviations depend on both wave age and steepness rather than varying monotonically with wave age. In particular, the models reproduce the mean velocity profiles with high accuracy for low steepness ($ak = 0.10$), with typical deviations below 12%. For slow-to-moderate waves ($c/u_* = 8, 10, 17$), however, deviations from MOW persist throughout the vertical extent. The logarithmic layer is well captured at $c/u_* = 21$ for all steepness values, whereas this agreement becomes less pronounced at very high wave age ($c/u_* = 24$) for moderate-to-high steepness, where the models underestimate the magnitude of momentum transfer into the mean flow.

Despite these quantitative differences, all three models capture the same qualitative trend in momentum transfer behavior. In particular, at high wave age (e.g., $c/u_* = 24$), all models indicate a reversal of momentum transfer from the waves to the airflow. However, the wave-phase-aware models do not fully reproduce the amplitude of the wave-induced velocity fluctuations resolved by the MOW model across any of the wave regimes considered.

The wave-phase-aware models reduce the vertical grid resolution requirements by approximately 10-20% in the present set of simulations while maintaining comparable accuracy to the MOW model. The computational cost of the MOW approach is approximately four times higher than that of the wave-phase-aware models, as it requires explicit resolution of the wave geometry and relies on double-precision (DP) computations. Double-precision increases memory usage and runtime compared with single-precision (SP) because more numerical accuracy is stored for each calculation. However, wave-phase-aware models

https://doi.org/10.5194/egusphere-2026-2292
Preprint. Discussion started: 2 June 2026

may require smaller timestep sizes under certain conditions, particularly in slow wave regimes, to maintain numerical stability in the WRF solver when the airflow velocity significantly exceeds the wave phase speed.

All simulations were performed using 32 CPU cores on a single compute node. The wall-clock time for the simulations ranged between approximately 12 and 36 hours, depending on the model fidelity and the wave regime considered. Simulations involving faster waves typically require longer integration times because of slower eddy turnover times, which increases the total simulation time needed to obtain statistically converged results.

Future work should aim to improve wave-phase-aware models to better represent the momentum transfer from waves to the wind across both fast wave (swell) regimes. In addition, the current WRF-LES implementations of WDM and WPM are limited to monochromatic wave conditions. Extensions to broadband wave modeling, recently developed as Dyn-WaSp for WDM (Aiyer et al., 2024) and SWARL for WPM (Ayala et al., 2026), are not included here and are left for future work.

Appendix A: Namelist options for the wave-phase-aware models (WRF-LES-WDM & WRF-LES-WPM)

Table A1 presents the available namelist options for the wave-phase-aware models in WRF-LES. The new namelist options were integrated into WRF by modifying the model registry for the wave-phase-aware modules, specifically `registry.wave_wdm` for the wave drag model (WRF-LES-WDM) and `registry.wave_wpm` for the windward potential flow model (WRF-LES-WPM), located in the main `Registry` directory. The wave-phase-aware models can be incorporated into WRF-LES by copying the relevant modules provided in the *Code and data availability* section of this manuscript, modifying a small number of associated files within the existing WRF directory structure, and recompiling the model. Monochromatic wave simulations in a channel flow configuration can then be performed using the appropriate namelist settings. Note that the current implementation requires disabling the surface layer schemes and driving the flow using a prescribed pressure gradient.

Code and data availability. The WRF model v3.8.1 is available at https://github.com/NCAR/WRFV3/releases (National Center for Atmospheric Research, 2017). The two wave-phase-aware models, named the Wave Drag Model (WDM) and the Windward Potential Flow Model (WPM) model implemented in WRF v3.8.1, together with the input files required to reproduce the case studies analyzed here, are archived on Zenodo (Kale and Howland (2026), https://doi.org/10.5281/zenodo.19357635).

Author contributions. The study was conceived by BK. Supplementary data from the LESGO code used for verification of the WDM implementation in WRF-LES were generated by MA and AKA. BK implemented the wave-phase-aware models into the WRF-LES model (v3.8.1) and conducted the simulations. The WDM was originally developed by AKA, while the WPM was adopted from existing work. MFH supervised the project. BK led the conceptualization and preparation of the initial manuscript draft, and all authors contributed to writing and revising the paper.

https://doi.org/10.5194/egusphere-2026-2292
Preprint. Discussion started: 2 June 2026

Table A1. Summary of WRF-LES-WDM and WRF-LES-WPM namelist options.

WRF-LES-WDM				
Namelist options (`&physics`)	Type	Default value	Unit	Description
`wdm_wave_opt` (max_domains)	`integer`	0	–	0: turn off Wave Drag Model (WDM), 1: monochromatic waves
`wdm_nwaves` (max_domains)	`integer`	5	–	Number of waves in the domain
`wdm_filter_vel` (max_domains)	`logical`	`.false.`	–	Turn on/off spatial test filtering at 2Δ for velocity
`wdm_filter_eta` (max_domains)	`logical`	`.false.`	–	Turn on/off spatial filtering at Δ for wave surface elevation
`wdm_ramp` (max_domains)	`logical`	`.false.`	–	Wave amplitude will be ramped up from zero using a `tanh` function
`wdm_drag_coeff_corr` (max_domains)	`logical`	`.false.`	–	Wave age-dependent drag coefficient correction for the transitional wave regime
`wdm_grad_analytical` (max_domains)	`logical`	`.false.`	–	Use an analytical solution to calculate the wave surface elevation gradients
`wdm_velocity_corr` (max_domains)	`logical`	`.false.`	–	Use geometry-dependent local velocity formulation (Equation (18)) as in Ayala et al. (2024)
`wdm_cst_P` (max_domains)	`real`	1.2	–	Constant P in drag coefficient, C_D
`wdm_cst_Q` (max_domains)	`real`	6.0	–	Constant Q in drag coefficient, C_D
`wdm_znts` (max_domains)	`real`	0.000001	m	Smooth wall roughness length scale
`wdm_amp` (max_domains)	`real`	0.0	m	Wave amplitude
`wdm_theta` (max_domains)	`real`	0.0	deg	Wave propagation direction
`wdm_phi` (max_domains)	`real`	0.0	deg	Wave phase angle, ϕ

WRF-LES-WPM				
Namelist options (`&physics`)	Type	Default value	Unit	Description
`wpm_wave_opt` (max_domains)	`integer`	0	–	0: turn off Windward Potential Flow Model (WPM), 1: monochromatic waves
`wpm_nwaves` (max_domains)	`integer`	5	–	Number of waves in the domain
`wpm_filter_vel` (max_domains)	`logical`	`.false.`	–	Turn on/off spatial test filtering at 2Δ for velocity
`wpm_filter_eta` (max_domains)	`logical`	`.false.`	–	Turn on/off spatial filtering at Δ for wave surface elevation
`wpm_ramp` (max_domains)	`logical`	`.false.`	–	Wave amplitude will be ramped up from zero using a `tanh` function
`wpm_grad_analytical` (max_domains)	`logical`	`.false.`	–	Use an analytical solution to calculate the wave surface elevation gradients
`wpm_znts` (max_domains)	`real`	0.000001	m	Smooth wall roughness length scale
`wpm_amp` (max_domains)	`real`	0.0	m	Wave amplitude
`wpm_theta` (max_domains)	`real`	0.0	deg	Wave propagation direction
`wpm_phi` (max_domains)	`real`	0.0	deg	Wave phase angle, ϕ

Competing interests. The authors declare that they have no conflict of interest.

Acknowledgements. BK and MFH gratefully acknowledge support from the Office of Naval Research, Young Investigator Program (YIP), grant no. N000142512045. Computational resources were provided by the Purdue Anvil HPC systems through NSF ACCESS projects ATM170028 and EVE240008. AKA was supported by an Early-Career Research Fellowship from the Gulf Research Program of the National Academies of Sciences, Engineering, and Medicine.

https://doi.org/10.5194/egusphere-2026-2292
Preprint. Discussion started: 2 June 2026

References

Aiyer, A. K., Deike, L., and Mueller, M. E.: A sea surface–based drag model for large-eddy simulation of wind–wave interaction, Journal of the Atmospheric Sciences, 80, 49–62, https://doi.org/10.1175/JAS-D-21-0329.1, 2023.

Aiyer, A. K., Deike, L., and Mueller, M. E.: A dynamic wall modeling approach for large eddy simulation of offshore wind farms in realistic oceanic conditions, Journal of Renewable and Sustainable Energy, 16, https://doi.org/10.1063/5.0159019, 2024.

Anderson, W.and Meneveau, C.: A large-eddy simulation model for boundary-layer flow over surfaces with horizontally resolved but vertically unresolved roughness elements, Boundary-layer meteorology, 137, 397–415, https://doi.org/10.1007/s10546-010-9537-5, 2010.

Arthur, R. S., Mirocha, J. D., Lundquist, K. A., and Street, R. L.: Using a canopy model framework to improve large-eddy simulations of the neutral atmospheric boundary layer in the weather research and forecasting model, Monthly Weather Review, 147, 31–52, https://doi.org/10.1175/MWR-D-18-0204.1, 2019.

Ayala, M., Sadek, Z., Ferčák, O., Cal, R. B., Gayme, D. F., and Meneveau, C.: A Moving Surface Drag Model for LES of Wind Over Waves: M. Ayala et al., Boundary-Layer Meteorology, 190, 39, https://doi.org/10.1007/s10546-024-00884-8, 2024.

Ayala, M., Gayme, D. F., and Meneveau, C.: Surface Wave-Aerodynamic Roughness Length Model for Air-Sea Interactions, Journal of the Atmospheric Sciences, p. e250146, https://doi.org/10.1175/JAS-D-25-0146.1, 2026.

Cao, T. and Shen, L.: A numerical and theoretical study of wind over fast-propagating water waves, Journal of Fluid Mechanics, 919, A38, https://doi.org/10.1017/jfm.2021.416, 2021.

Charnock, H.: Wind stress on a water surface, Quarterly Journal of the Royal Meteorological Society, 81, 639–640, https://doi.org/10.1002/qj.49708135027, 1955.

Desjardins, O., Blanquart, G., Balarac, G., and Pitsch, H.: High order conservative finite difference scheme for variable density low Mach number turbulent flows, Journal of Computational Physics, 227, 7125–7159, https://doi.org/10.1016/j.jcp.2008.03.027, 2008.

Donelan, M. A.: Air–Sea Interaction, in: The Sea—Ideas and Observations on Progress in the Study of the Seas, edited by LeMehaute, B. and Hanes, D. M., vol. 9B of *Ocean Engineering Science*, pp. 239–292, John Wiley and Sons, 1990.

Fairall, C. W., Bradley, E. F., Hare, J. E., Grachev, A. A., and Edson, J. B.: Bulk parameterization of air–sea fluxes: Updates and verification for the COARE algorithm, Journal of Climate, 16, 571–591, https://doi.org/10.1175/1520-0442(2003)016<0571:BPOASF>2.0.CO;2, 2003.

Hara, T. and Sullivan, P. P.: Wave boundary layer turbulence over surface waves in a strongly forced condition, Journal of Physical Oceanography, 45, 868–883, https://doi.org/10.1175/JPO-D-14-0116.1, 2015.

Husain, N. T., Hara, T., and Sullivan, P. P.: Wind turbulence over misaligned surface waves and air–sea momentum flux. Part I: Waves following and opposing wind, Journal of Physical Oceanography, 52, 119–139, https://doi.org/10.1175/JPO-D-21-0043.1, 2022.

Kale, B. and Howland, M. F.: Wave-phase-aware model implementations in WRFV3-3.8.1 (code and simulation files), https://doi.org/10.5281/zenodo.19357635, 2026.

Kihara, N., Hanazaki, H., Mizuya, T., and Ueda, H.: Relationship between airflow at the critical height and momentum transfer to the traveling waves, Physics of Fluids, 19, https://doi.org/10.1063/1.2409736, 2007.

Liu, Y., Yang, D., Guo, X., and Shen, L.: Numerical study of pressure forcing of wind on dynamically evolving water waves, Physics of Fluids, 22, https://doi.org/10.1063/1.3414832, 2010.

MacArt, J. F. and Mueller, M. E.: Semi-implicit iterative methods for low Mach number turbulent reacting flows: Operator splitting versus approximate factorization, Journal of Computational Physics, 326, 569–595, https://doi.org/10.1016/j.jcp.2016.09.016, 2016.

https://doi.org/10.5194/egusphere-2026-2292
Preprint. Discussion started: 2 June 2026

Meneveau, C.: A note on fitting a generalised Moody diagram for wall modelled large-eddy simulations, Journal of Turbulence, 21, 650–673, https://doi.org/10.1080/14685248.2020.1840573, 2020.

Porchetta, S., Temel, O., Muñoz-Esparza, D., Reuder, J., Monbaliu, J., Van Beeck, J., and van Lipzig, N.: A new roughness length parameterization accounting for wind–wave (mis) alignment, Atmospheric Chemistry and Physics, 19, 6681–6700, https://doi.org/10.5194/acp-19-6681-2019, 2019.

Skamarock, W. C. and Klemp, J. B.: A time-split nonhydrostatic atmospheric model for weather research and forecasting applications, Journal of computational physics, 227, 3465–3485, https://doi.org/10.1016/j.jcp.2007.01.037, 2008.

Sullivan, P. P., McWilliams, J. C., and Moeng, C.-H.: Simulation of turbulent flow over idealized water waves, Journal of Fluid Mechanics, 404, 47–85, https://doi.org/10.1017/S0022112099006965, 2000.

Sullivan, P. P., Banner, M. L., Morison, R. P., and Peirson, W. L.: Turbulent flow over steep steady and unsteady waves under strong wind forcing, Journal of Physical Oceanography, 48, 3–27, https://doi.org/10.1175/JPO-D-17-0118.1, 2018.

Taylor, P. K. and Yelland, M. J.: The dependence of sea surface roughness on the height and steepness of the waves, Journal of physical oceanography, 31, 572–590, https://doi.org/10.1175/1520-0485(2001)031<0572:TDOSSR>2.0.CO;2, 2001.

Yang, D. and Shen, L.: Direct-simulation-based study of turbulent flow over various waving boundaries, Journal of Fluid Mechanics, 650, 131–180, https://doi.org/10.1017/S0022112009993557, 2010.

Zhu, P., Li, T., Mirocha, J. D., Arthur, R. S., Wu, Z., and Fringer, O. B.: A moving-wave implementation in WRF to study the impact of surface water waves on the atmospheric boundary layer, Monthly Weather Review, 151, 2883–2903, https://doi.org/10.1175/MWR-D-23-0077.1, 2023.